Focusing and imaging properties of diffractive optical elements with star-ring topological structure

Jie Ke[a, b], Junyong Zhang*[a], Yanli Zhang[a], Meizhi Sun[a]
[a]Shanghai Institute of Optics and Fine Mechanics, Chinese Academy of Sciences, Shanghai 201800, China; [b]University of Chinese Academy of Sciences, Beijing 100049, China

ABSTRACT

A kind of diffractive optical elements (DOE) with star-ring topological structure is proposed and their focusing and imaging properties are studied in detail. The so-called star-ring topological structure denotes that a large number of pinholes distributed in many specific zone orbits. In two dimensional plane, this structure can be constructed by two constrains, one is a mapping function, which yields total potential zone orbits, corresponding to the optical path difference (OPD); the other is a switching sequence based on the given encoded seed elements and recursion relation to operate the valid zone orbits. The focusing and imaging properties of DOE with star-ring topological structure are only determined by the aperiodic sequence, and not relevant to the concrete geometry structure. In this way, we can not only complete the traditional symmetrical DOE, such as circular Dammam grating, Fresnel zone plates, photon sieves, and their derivatives, but also construct asymmetrical elements with anisotropic diffraction pattern. Similarly, free-form surface or three dimensional DOE with star-ring topological structure can be constructed by the same method proposed. In consequence of smaller size, lighter weight, more flexible design, these elements may allow for some new applications in micro and nanphotonics.

Keywords: diffractive optics, star-ring topology, mapping function, switching sequence, Fibonacci

1. INTRODUCTION

In photonics technology, diffractive optical elements (DOE) have found a large number of new applications in many different areas, covering the whole electromagnetic spectrum from X-ray microscopy to THz imaging. Specially, focusing and imaging of soft or hard X-ray and ultraviolet (EUV) have many applications in physical and life sciences. However, conventional refractive lens are impossible to focus X-ray and EUV in consequence of strong absorption of solid materials. Traditional Fresnel zone plates can be used for this kind of focusing [1, 2], but its resolution is limited by the width of outmost zone [3, 4]. In 2001, Kipp *et al.* proposed photon sieves [5], where a zone plate originally composed of concentric rings is arranged properly by a great number of pinholes. This new DOE has caused wide public concern over the recent years [6-8] and researchers have designed different kinds of DOE [9-15] based on photon sieves proposed by Kipp *et al*..

Fibonacci sequence, named with the inventor Italian mathematician Leonardo de Pisa, called Fibonacci, has been employed in the development of different photonic devices. The focusing and imaging properties of Fibonacci diffractive elements, *e.g.*, gratings [16-18], lenses [19-21], zone plates[22], *etc*., are studied in detail. But this amazing aperiodic sequence isn't yet applied in photon sieves.

In this paper, we propose a type of DOE with star-ring topological structure. The geometry of this kind of DOE based on pinholes has two constrains. One is a mapping function of OPD, which controls the radii of total potential zone orbits; the other is a switching sequence generated by the encoded generalized Fibonacci sequence. The focusing and imaging properties are only determined by the switching sequence, and not relevant to the optical structure parameters. Since the star-ring topological DOE has special focusing and imaging properties, such as on-axis multi-foci, adjustable ratio of multifocal lengths, anisotropic diffraction pattern and outstanding transverse resolution, it may allow for many applications in nanometer lithography [23], weapons vision [24], spectroscopy.

* zhangjin829@163.com

2015 International Conference on Optical Instruments and Technology: Micro/Nano Photonics and Fabrication, edited by Zhiping Zhou, Changhe Zhou, Pavel Cheben, Proc. of SPIE Vol. 9624, 962403 · © 2015 SPIE
CCC code: 0277-786X/15/$18 · doi: 10.1117/12.2190171

2. STAR-RING TOPOLOGICAL DOE DESIGN

2.1 Star-ring topological DOE

The basic unit of star-ring topological DOE is pinhole, which arranges properly on a zone orbit originally composed of concentric circular or rectangular rings shown in Figure 1. This concept is similar to photon sieves. Whereas, overlapping pinholes are avoided and considered as a destructive factor in traditional photon sieves. In fact, completely overlapping pinholes over the innermost zones or outmost zones can be considered as zone plates to form Gaussian apodized photon sieves [25] or compound photon sieves [26]. And partly overlapping pinholes are also allowed in this DOE.

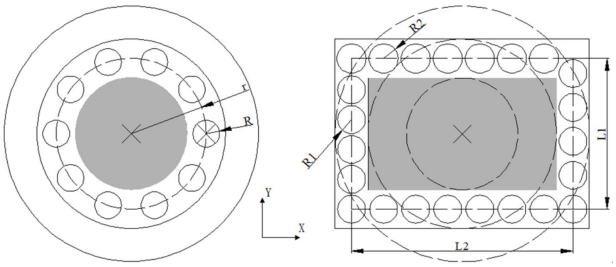

Figure 1. Schematic of a planar star-ring topological DOE. (a) Polar coordinate. (b) Cartesian coordinate.

Considering two extreme cases, one is that completely overlapping pinholes distributed in all own orbits to form traditional zone plates; the other is completely separate pinholes in star-ring topological DOE which can be called traditional photon sieves. Besides, the design of Fibonacci grating [16] and Fibonacci zone plates [22] makes it possible that photon sieves may be designed on these new zone plates taking the place of Fresnel zone plates which is based on half wave method. This method indicates that the OPD between two adjacent zone orbits is 0.5 λ.

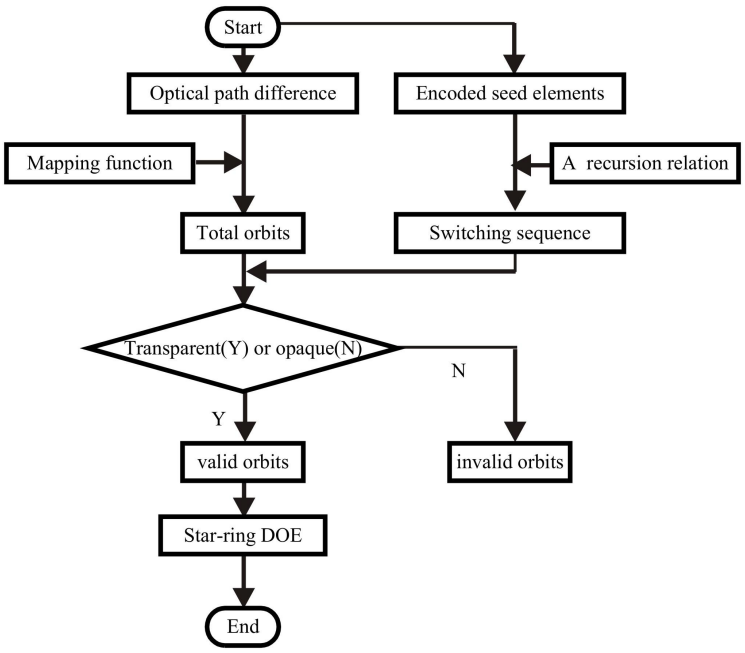

Figure 2. Flow chart of designing star-ring topological DOE.

In fact, these DOEs including Fresnel zone plates and photon sieves above can be constructed by two constrains, one is OPD, which yields total potential zone orbits; the other is a switching sequence based on given seed elements and recursion relation with respect to valid zone orbits. Figure 2 shows the design flow of star-ring topological DOE. No

matter whether zone plates, photon sieves or their derivatives, we call this kind of DOE based on pinholes star-ring topological DOE.

2.2 Mapping function corresponding to optical path difference

There are many mapping functions to control the radii of total zone orbits, but here OPD between zone orbits is mainly discussed. As shown in Figure 3, a point light source is incident on the star-ring topological DOE, and the OPD between upper wavelet (*ABC*) and the center wavelet (AOC) can be described as

$$OPD_m = \sqrt{L^2 + r_m^2} + \sqrt{F^2 + r_m^2} - L - F, m \in N \tag{1}$$

where r_m denotes the radius of the mth zone orbit, L is the distance from the light source to DOE and F is the expected focal distance.

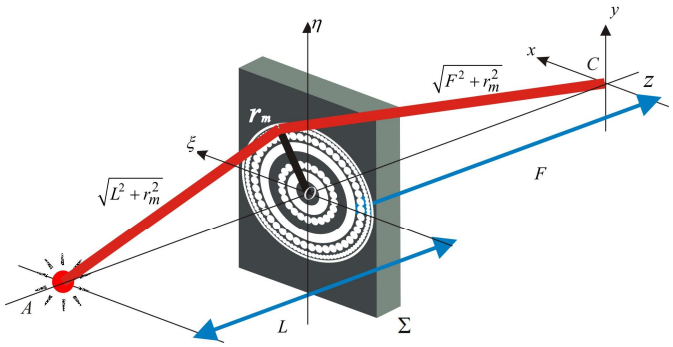

Figure 3. Diffraction model by star-ring topological DOE.

Now let us discuss again the approach to generating zone orbits of traditional Fresnel zone plates and photon sieves. As is well-known to us, the OPD divided by dichotomy between their two adjacent zone orbits is 0.5λ. In other words, the single period of OPD is 0.5λ. However, if we alter the period as $K\lambda$ shown in Figure 4, the diffractive optical lever appears, but the ratio of multi-focal distances remains the same, which will be discussed Section 3.2. Moreover, if the OPD between several zone orbits is periodic and the whole period is still $K\lambda$ but divided into several segments as $M_1\lambda$, $M_2\lambda$, $M_3\lambda$, $\cdots$, $M_j\lambda$ ($0 \le M_1 < M_2 < \cdots < M_j < K$) shown in Figure 4(a), this OPD between adjacent zone orbits is aperiodic.

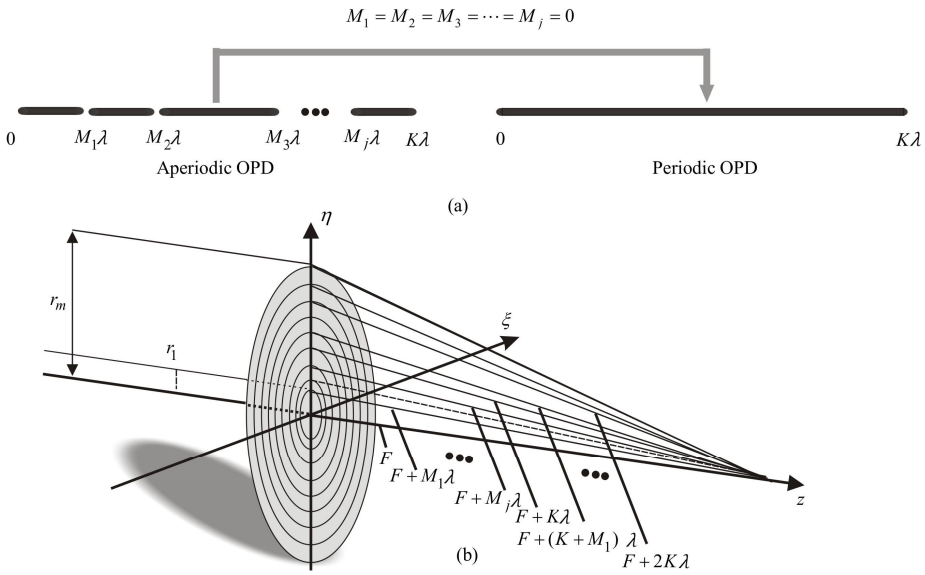

Figure 4. Optical path of zone orbits of star-ring topological DOE under parallel light irradiation.

For periodic OPD (M_j=0), the value of OPD_m can be further expressed as

$$OPD_m = mK\lambda, m \in N, K \in R_+ \tag{2}$$

In this way, one can express the radius of the mth zone orbit in Eq. (1) as

$$r_m = \sqrt{(mK\lambda)^2 + 2mK\lambda F} \tag{3}$$

But for aperiodic OPD, the radius of the mth zone orbit can be got by recursive method. Circular Dammann grating [27] can be seen as a specific example of aperiodic OPD, whose whole period $K\lambda$ is normalized and divided into many segments corresponding to its order, but the values of M_j are optimized.

2.3 Switching sequence with respect to generalized Fibonacci sequence

The mapping function determined by OPD produces total potential zone orbits of star-ring topological DOE, but whether pinholes are distributed in the zone orbits, one should consider the switching sequence. Switching sequence is generated by encoded seed elements and recursion relation. Here we mainly take generalized Fibonacci sequence [28] into account. For the standard Fibonacci sequence

$$1,1,2,3,5,8,13,21,34,55,89,144,233,377\cdots \tag{4}$$

defined by the linear recursion relation $F_n=F_{n-1}+F_{n-2}$ with two seed elements F_1=1, F_2=1. The golden mean is defined as the limit of the ratio of two consecutive Fibonacci numbers.

Suppose we alter the initial seed elements as $F_1=a$, $F_2=b$ ($a, b \in N^*$), then generalized Fibonacci sequence can be defined by the corresponding linear recursion relation modified as

$$F_{n+2} = pF_{n+1} + qF_n, p, q, n \in N_+ \tag{5}$$

Based on generalized Fibonacci recursion relation, switching sequence can also be generated with two encoded seed elements. Taking the standard Fibonacci recursion relation as an example, after encoding two seed elements F_1=1, F_2=1 as (F^1, F^2)=(1,0), 8-order switching sequence F^8 should be 01001010010101001010, where 1 denotes valid zone orbits and 0 is invalid ones. That means the number of total potential zone orbits is 21 and the number of valid zone orbits is 8. Taking traditional half wave zone method (M_j=0, K=0.5) into account, then based on Eq. (3) one can design different star-ring topological DOE. Figure 5 shows this kind of DOE with completely overlapping pinholes (standard Fibonacci zone plates), partly overlapping pinholes, and completely separate pinholes (standard Fibonacci photon sieves).

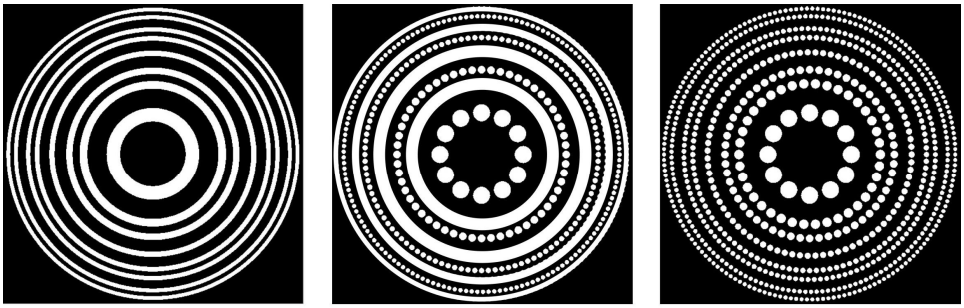

(a) (b) (c)

Figure 5. Some standard Fibonacci star-ring topological DOE (F^8 in this case). (a) Completely overlapping pinholes. (b) Partly overlapping pinholes. (c) Completely separate pinholes.

Generally, in order to get expected focusing and imaging properties, the radii of pinholes at different valid zone orbits should be optimized similar to the one Kipp *et al.* did in 2001 [5].

2.4 Diffraction model

As described above, the diffraction properties of generalized Fibonacci star-ring topological DOE is the main concern in this paper. The relation of focal distances and the ratio of compression of focal spot in different directions are only determined by the switching sequence, and not relevant to the geometry structure of star-ring topological DOE. We will investigate focusing and imaging properties of two extreme examples, *i.e.*, generalized Fibonacci zone plates (see Figure 5(a)) and photon sieves (see Figure 5(c)) and their transition (see Figure 5(b)).

Theoretically, when a monochromatic plane wave is incident on the pinhole on the mth valid orbit, whose central location and radii are denoted by (ξ_{mn}, η_{mn}) and r_{mn}, their transmission function can expressed as $t_{mn}(\xi, \eta)$=circ[$(\xi-\xi_{mn})/r_{mn}$,$(\eta-\eta_{mn}) / r_{mn}$]. Based on the Huygens-Fresnel principle, its diffraction field can be formulated as below:

$$U_{mn}(x,y) = \frac{z}{i\lambda}\iint_{\Sigma} t_{mn}(\xi,\eta)\frac{\exp(ikR_{mn})}{R_{mn}}\mathrm{d}\xi\mathrm{d}\eta \tag{6}$$

where k is the wave number, R_{mn} is the distance between point (ξ, η, 0) and point (x, y ,z), i is the imaginary unit, and n denotes the number of pinholes on the mth valid orbit.

According to the linear superposition principle, the total diffracted field $U_{total}(x, y)$ of star-ring topological DOE is the simple sum of those individual diffracted fields from different pinholes. That is to say, the total diffracted field can be described as

$$U_{total}(x,y) = \sum_{m}\sum_{n} U_{mn}(x,y) \tag{7}$$

Besides, scalar diffraction theory is valid when the size of pinhole is larger than five times of wavelength. Here wavelength λ is 632.8nm and the expected focal length F equals to 3.554cm. The two parameters will remain the same. And in the paper, F_1=2 and F_2=3 are the initial seed elements.

3. THE ON-AXIS INTENSITY DISTRIBUTION OF GENERALIZED FIBONACCI ZONE PLATES

3.1 The same optical path difference and different switching sequence

For the purposes of our discussion, the value of K in Eq. (3) is equal to 0.5 and M_j is 0 in this situation but switching sequences are different. The switching sequence is determined by encoded seed elements and recursion relation.

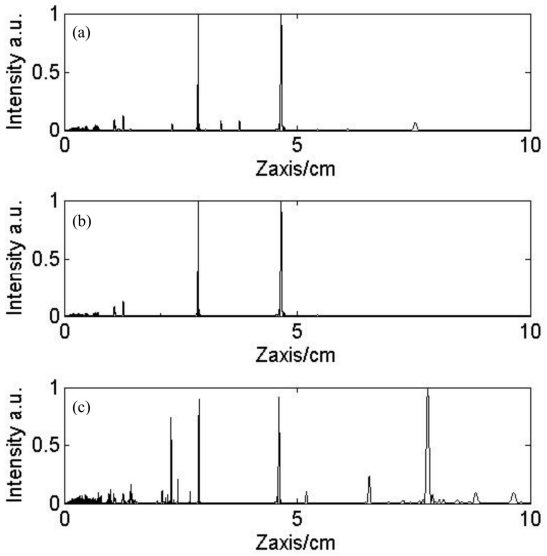

Figure 6. On-axis intensity produced by standard Fibonacci zone plates against the axial distance z (F^{12} in this case). (a) (F^1, F^2)=(01,010). (b) (F^1, F^2)=(11,010). (c) (F^1, F^2)=(11,001).

First, let us discuss the standard Fibonacci linear recursion relation with different encoded seed elements. Figure 6 shows the on-axis intensity distribution of three kinds of encoded seed elements: (F^1, F^2)=(01,010), (F^1, F^2)=(11,010), and (F^1, F^2)=(11,001).

For bifocal standard Fibonacci zone plates shown in Figure 6 (a) and (b), they can present two equal intensity foci and that the two focal distances are 2.873cm and 4.655cm. Obviously, the ratio of the two focal distances approaches the golden mean. Besides, it implies that there exists better encoded seed elements with few secondary foci at the same

conditions. It also suggests that Fibonacci zone plates with different switching sequences maybe present the same axial intensity distribution. However, as it shows in Figure6 (c), this DOE may also present four foci on the two sides of expected focus. It is imperative that in order to get bifocal Fibonacci zone plates with the ratio of two focal distances approaching to golden mean, the encoded seed elements should be sifted.

Now keep encoded seed elements (F^1, F^2)=(01,010) but alter linear recursion relation by changing the value of p and q in Eq. (5). Figure 7 shows on-axis intensity produced by generalized Fibonacci zone plates with q=1 and p=1, p=2, p=3, respectively. They still present two equal intensity foci on the two sides of expected focus, but the ratio of two focal distances changes from 0.617 to 0.585 and 0.556 due to the different switching sequences. It suggests that the ratio of two focal distances can be altered, which is different with Ref. [20].

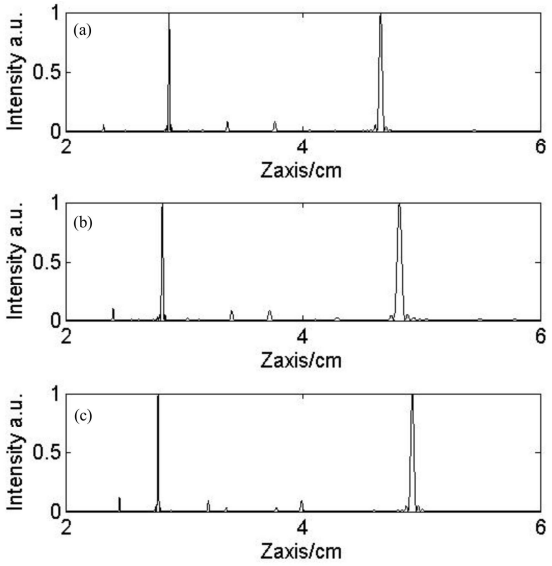

Figure 7. On-axis intensity produced by generalized Fibonacci zone plates against the axial distance z with encoded seed elements (F^1, F^2)=(01,010) (F^8 in this case). (a) p=1, q=1. (b) p=2, q=1. (c) p=3, q=1.

3.2 The same switching sequence and different optical path difference

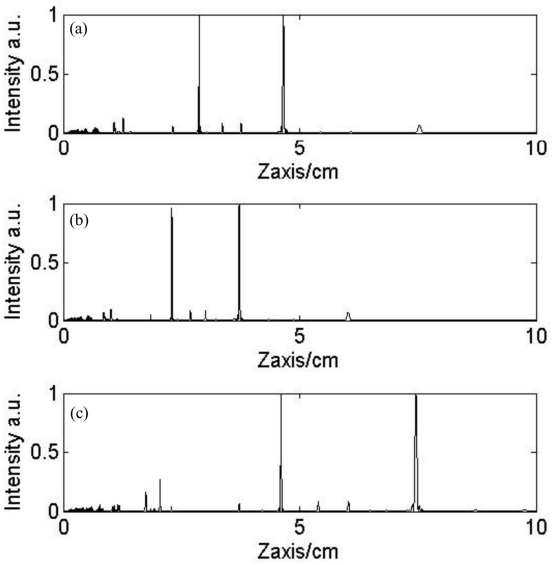

Figure 8. On-axis intensity produced by standard Fibonacci zone plates against the axial distance z with encoded seed elements (F^1, F^2)=(01,010). (a) K= 0.5. (b) K= 0.4. (c) K= 0.8.

As an example for reference, the simulation parameters of standard Fibonacci zone plates in this situation are as follows: K=0.5, M_j=0, (F^1, F^2)=(01,010), p=1 and q=1, whose axial field diffraction distribution is shown in Figure 8 (a). Then one can alter the OPD between two adjacent zone orbits to form different kinds of Fibonacci zone plates. When K is equal to 0.4, the two focal distances are changed as 2.296*cm* and 3.722*cm* shown in Figure 8 (b). And when K is equal to 0.8, the two focal distances are changed as 4.605*cm* and 7.459*cm* shown in Figure 8 (c). What is interesting is that the magnification or minification bifocal distances is exactly equal to the ratio of the two values of K, such as 2.296/4.605≈0.4/0.8.

Hence, in this way, one can regulate and control the distribution of two foci to a certain degree. However, the value of K can't be changed arbitrarily. Too big or too small value of K may destroy the focusing and imaging properties.

3.3 Abnormal phenomenon of depth of secondary foci

In this section, we discuss an abnormal phenomenon of depth of secondary foci. The parameters are as follows: wavelength λ is 632.8*nm* and the expected focal length F equals to 3.554*cm*. Taking Fresnel zone plates into account, Figure 9 indicates that the depth of the principal focus will decrease as the number of zones increases. In contrast, the first minor focus will be splitted into multiple parts with increment of the radius of Fresnel zone plates. This results to increment of the depth of focus, but the zero position of the trailing edge of the minor focus retains the same. Generally speaking, the depth of focus is proportional to λ/N.A.^{2}. It's an abnormal phenomenon for minor focus, but the principal focus is normal. For axial multiple foci, abnormal phenomenon can be used for differentiating the principal foci from the minor foci. This phenomenon also exists in generalized Fibonacci zone plates above.

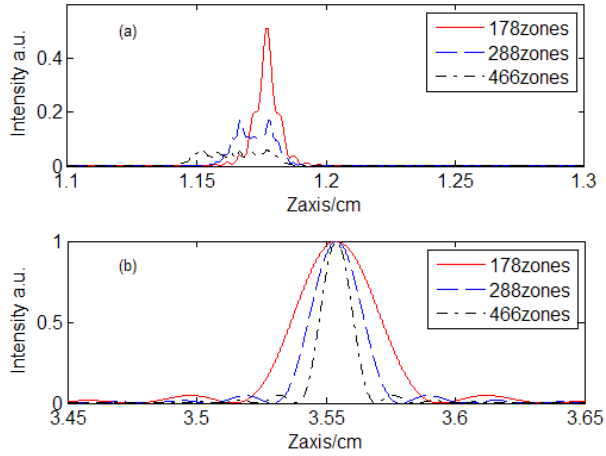

Figure 9. Axial intensity by conventional Fresnel zone plates. (a) The first minor focus, (b) the principal focus.

4. FIBONACCI PHOTON SIEVE BY TWO DIFFERENT CONSRTAINS

Now consider another extreme situation, where there are completely separate pinholes in valid zone orbits. We can call this kind of DOE Fibonacci photon sieves which has more flexible design. All kinds of structure of star-ring topological DOE mentioned above are rotationally symmetric, so the intensity of focal spot in the focal planes is isotropic. In order to fulfill anisotropic focusing, asymmetric structure is introduced into star-ring topological DOE. The simplest way is to simultaneously operate mapping or switching sequence in two directions, such as on both x-axis and y-axis.

Figure 10 indicates that the schematic of rectangular Fibonacci photon sieves which consists of a series of concentric rectangular orbits and square orbits. No matter on y-axis or on x-axis, the production rule of switching sequence satisfies standard Fibonacci recursion relation with p=q=1 and K is equal to 1. But on y-axis, M_1 (j=1) is equal to 0.25 and the encoded seed elements is (01, 010) while on x-axis, M_1 (j=1) is equal to 0.5 and the encoded seed elements is (00, 001).

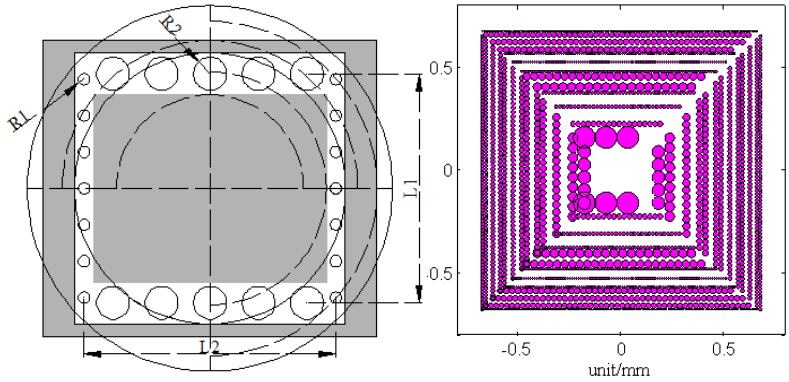

Figure 10. Schematic of rectangular Fibonacci photon sieves composed of concentric rectangular orbits and square orbits.

The total number of total potential zone orbits is 89 on y-axis and on x-axis, respectively. There are 34 valid zone orbits on y-axis, while 21 valid zone orbits on x-axis. So the total number of valid zone orbits of this star-ring topological DOE is 55 on account of no overlapping. Figure 11 depicts the normalized axial intensity distribution with different ratio of *d/w* by shooting method, where *d* is the diameter of pinhole, and *w* is the width of its corresponding valid zone orbit. The two focal distances are 2.875*cm* and 4.665*cm* at *d/w*=1, respectively. When *d/w*=0.81, we can obtain two approximately equal intensity foci on z-axis. But beyond that, the third focus emerges, whose intensity has risen an astonishing 66.6 percent of the peak value of the principal maximum. Meanwhile, one of the more remarkable aspects of this kind of star-ring topological DOE is that the main two axial foci are all asymmetrical in consequence of the asymmetry of optical device. Moreover, depth of two principal foci has increased with the increment of ratio *d/w*.

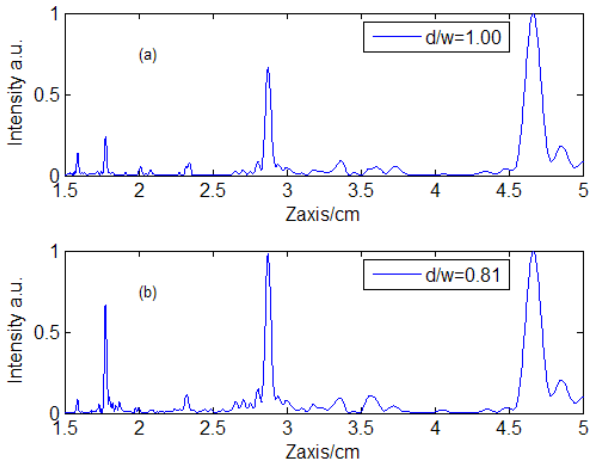

Figure 11. Axial intensity distribution with different ratio of *d/w*: (a) *d/w*=1, (b) *d/w*=0.81.

Then we investigate the transverse intensity distribution on the focal plane. Figure 12 shows the transverse bifocal intensity distribution. The irradiance displays obvious anisotropy. For the first focus, FWHM (the full width half maximum) is 7.90μm on x-axis and 10.31μm on y-axis, respectively. The compression ratio of width on x-axis to that on y-axis is 0.76. And for the second focus, FWHM is 12.88μm and 13.56μm. Its corresponding compression ratio is 0.95. In addition, because of standard Fibonacci recursion relation, the ratio of the first focal width on x-axis to the second focal width equals to 0.6134 that is quite close to golden mean.

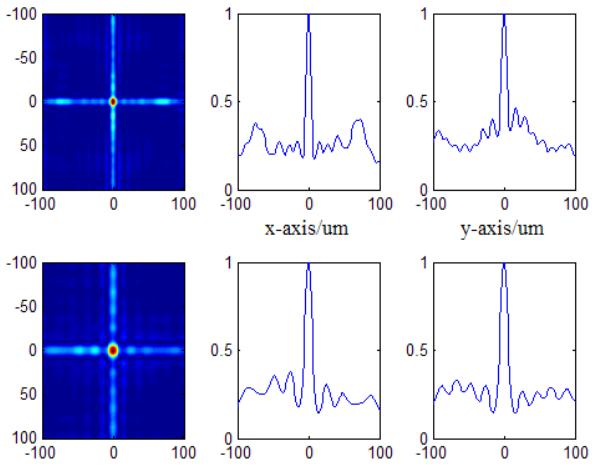

Figure 12. Transverse bifocal intensity distribution on the focal plane

5. TRANSVERSE RESOLUTION OF THREE TYPICAL STAR-RING TOPOLOGICAL DOES

By optimizing the radii of pinholes, Fibonacci photon sieves can present axial focusing properties similar to Fibonacci zone plates discussed in Section 3.

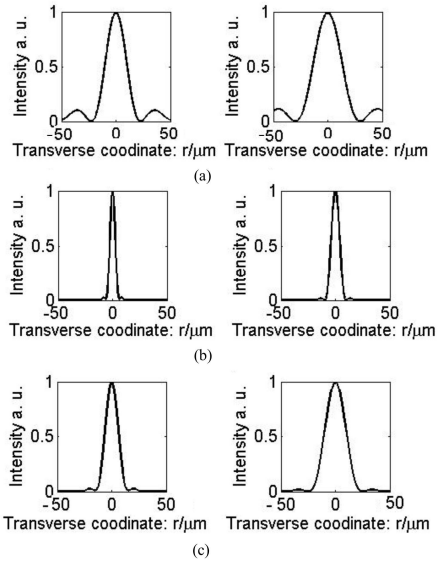

Figure 13. Normalized transverse intensity distribution on the bifocal plane of three typical star-ring topological DOEs (F^{10} in this case). (a) Standard Fibonacci zone plates. (b) Compound Fibonacci zone plates and photon sieves. (c) Standard Fibonacci photon sieves.

Here we still use standard Fibonacci zone plates (see Figure 5 (a)) as reference, whose axial field diffraction distribution is shown in Figure 6 (a). With the same simulation parameters, transverse resolution of compound Fibonacci zone plates and photon sieves (see Figure 5 (b)) and standard Fibonacci photon sieves (see Figure 5 (c)) are studied.

Three types of transverse intensity computed for Fibonacci zone plates, associated compound Fibonacci zone plates and standard Fibonacci photon sieves are shown in Figure 13. Compared with Fibonacci zone plates which is composed of completely overlapping pinholes, Fibonacci photon sieves have better resolution with few sidelobes. But, the transverse resolution of compound Fibonacci zone plates and photon sieves has been greatly improved. Meanwhile, we also discover that the transverse resolution of second DOE can be adjusted from that of Fibonacci zoon plates to that of Fibonacci photon sieves by altering the number of completely overlapping pinholes.

6. CONCLUSION

We developed one kind of diffractive optical elements with star-ring topological structure and studied its focusing and imaging properties. Then we proposed the approach to design star-ring topological DOE by two constrains, *i.e.*, mapping function and switching sequence. OPD was chosen as mapping function to control the radii of total potential zone orbits, where pinholes may be distributed, and generalized Fibonacci sequence was chosen as switching sequence to get valid zone orbits, where pinholes are really distributed. The ratio of multi-focal distances and the compression ratio of focal spots in different directions is only determined by the switching sequence, and not relevant to the concrete geometry structure of star-ring topological DOE. Simulation results showed that this kind of DOE had some distinctive optical characteristics, such as multiple foci, anisotropic diffractive pattern, and better resolution on multifocal plane.

ACKNOWLEDGEMENT

This research is supported by the National Natural Science Foundation of China (No. 61205212, 61205210).

REFERENCES

[1] Kirz, J., "Phase zone plates for x rays and the extreme uv," J. Opt. Soc. Am., 64(3), 301-309 (1974).

[2] Adnderson, E. H., Boegli, V., and Muray, L. P., "Electron beam lithography digital pattern generator and electronics for generalized curvilinear structures," J. Vac. Sci. Techol. B, 13, 2529-2534 (1995).

[3] Kyuragi, H., and Urisu, T., "Higher-order suppressed phase zone plates," Appl. Opt., 24(8), (1985).

[4] Sun, J. A., and Cai, A., "Archaic focusing properties of Fresnel zone plates," J. Opt. Soc. Am. A, 8, 33-35 (1991).

[5] Kipp, L., Skibowski, M., Johnson, R. L. *et al.*, "Sharper images by focusing soft X-rays with photon sieves," Nature, 414, 184-187 (2001).

[6] Cao, Q., and Jahns, J., "Focusing analysis of the pinhole photon sieve: individual far field model," J. Opt. Soc. Am. A, 19(12), 2387-2393 (2002).

[7] Cao, Q., and Jahns, J., "Nonparaxial model for the focusing of highnumerical-aperture photon sieves," J. Opt. Soc. Am. A, 20(6), 1005-1012 (2003).

[8] Zhang, J., Cao, Q., Lu, X. *et al.*, "Focusing contribution of individual pinholes of a photon sieve_dependence on the order of local ring of underlying traditional Fresnel zone plate," Chin. Opt. Lett., 8(1), 256-258 (2010).

[9] Giménez, F., Monsoriu, J. A., and Pons, W. D. F. a. A., "Fractal photon sieve," Opt. Express, 14(25), 11958-11963 (2006).

[10] Jia, J., and Xie, C., "Phase zone photon sieve," Chin. Phys. B, 18(1), 183-188 (2009).

[11] Andersen, G., "Membrane Photon sieve Telescopes," Proc. SPIE, 7731, 7731-1-7731-8 (2010).

[12] Cheng, G., Hu, C., Xu, P. *et al.*, "Zernike apodized photon sieves for high-resolution phase-contrast X-ray microscopy," Opt. Lett., 35(21), 3610-3612 (2010).

[13] Xie, C., Zhu, X., Shi, L. *et al.*, "Spiral photon sieves apodized by digital prolate spheroidal window for the generation of hard-x-ray vortex," Opt. Lett., 31, 1756-1766 (2010).

[14] Zhang, J., Cao, Q., Lu, X. *et al.*, "Individual far-field model for photon sieves composed of square pinholes," JOSA A, 27(6), 1342-1346 (2010).

[15] Kalläne, M., Buck, J., Harm, S. *et al.*, "Focusing light with a reflection photon sieve," Opt. Lett., 36, 2405-2407 (2011).

[16] Gao, N., Zhang, Y., and Xie, C., "Circular Fibonacci gratings," Appl. Opt., 50(31), G142-G148 (2011).

[17] Verma, R., Banerjee, V., and Senthilkumaran, P., "Fractal signatures in the aperiodic Fibonacci grating," Opt. Lett., 39(9), 2257-2260 (2014).

[18] Verma, R., Sharma, M. K., Senthilkumaran, P. *et al.*, "Analysis of Fibonacci gratings and their diffraction patterns," J. Opt. Soc. Am. A, 31(7), 1473-1480 (2014).

[19] Calatayud, A., Ferrando, V., Remon, L. *et al.*, "Twin axial vortices generated by Fibonacci lenses," Opt. Express, 21(8), 10234-10239 (2013).

[20] Monsoriu, J. A., Calatayud, A., Remon, L. *et al.*, "Bifocal Fibonacci Diffractive Lenses," IEEE Photonics Journal, 5(3), 3400106 (2013).

[21] Ferrando, V., Calatayud, A., Andres, P. *et al.*, "Imaging Properties of Kinoform Fibonacci Lenses," IEEE Photonics Journal, 6(1), 6500106 (2014).

[22] Dai, H. T., Liu, Y. J., and Sun, X. W., "The focusing property of the spiral Fibonacci zone plate," Proc. SPIE, 8257, 82570T (2012).
[23] Gil, R. M. a. D., Barbastathis, G., and Smith, H. I., "Photon-sieve lithography," J. Opt. Soc. Am. A, 22(2), 342-345 (2005).
[24] Kincade, K., "Photon sieves enhance weapons vision," Laser Focus World, 40(3), 34-37 (2004).
[25] Sabatyan, A., and Roshaninejad, P., "Super-resolving random-Gaussian apodized photon sieve," Appl. Opt., 51(26), 6315-6318 (2012).
[26] Xie, C., Zhu, X., Li, H. *et al.*, "Feasibility study of hard-x-ray nano focusing above 20 keV using compound photon sieves," Opt. Lett., 35(23), 4048-4050 (2010).
[27] Zhou, C., Jia, J., and Liu, L., "Circular Dammann grating," Opt. Lett., 28(22), 2174-2176 (2003).
[28] Horadam, A. F., "A generalized Fibonacci sequence," The American Mathematical Monthly, 68(5), 455-459 (1961).